Atmos. Chem. Phys. Discuss., 15, 9507–9540, 2015
www.atmos-chem-phys-discuss.net/15/9507/2015/
doi:10.5194/acpd-15-9507-2015

Atmospheric Chemistry and Physics Discussions

Aerosol vertical distribution, optical properties and transport over Corsica (western Mediterranean)

J.-F. Léon[1], P. Augustin[2], M. Mallet[1], T. Bourrianne[3], V. Pont[1], F. Dulac[4], M. Fourmentin[2], D. Lambert[1], and B. Sauvage[1]

[1]Laboratoire d'aérologie, CNRS, Université Paul Sabatier, Toulouse, France
[2]Laboratoire de physico-chimie de l'atmosphère, Université du Littoral Côte d'Opale, Dunkerque, France
[3]Centre National de la recherche météorologique, CNRS, Météo-France, Toulouse, France
[4]Laboratoire des sciences du climat et de l'environnement, UMR8212 CEA-CNRS-UVSQ, Gif-Sur-Yvette, France

Received: 26 January 2015 – Accepted: 13 March 2015 – Published: 31 March 2015

Correspondence to: J.-F. Léon (jean-francois.leon@aero.obs-mip.fr)

Published by Copernicus Publications on behalf of the European Geosciences Union.

Abstract

This paper presents the aerosol vertical distribution observed in the western Mediterranean between February and April 2011 and between February 2012 and August 2013. An elastic backscattering lidar was continuously operated at a coastal site in the northern part of Corsica Island (Cap Corse) for a total of more than 14 000 h of observations. The aerosol extinction coefficient retrieved from cloud-free lidar profiles are analyzed along with the SEVIRI satellite aerosol optical depth (AOD). The SEVIRI AOD was used to constrain the retrieval of the aerosol extinction profiles from the lidar range-corrected signal and to detect the presence of dust or pollution aerosols. The daily average AOD at 550 nm is 0.16 (±0.09) and ranges between 0.05 and 0.80. A seasonal cycle is observed with minima in winter and maxima in spring–summer. High AOD days (above 0.3 at 550 nm) represent less than 10 % of the totality of daily observations and correspond to the large scale advection of desert dust from Northern Africa or pollution aerosols from Europe. The respective origin of the air masses is confirmed using FLEXPART simulations in the backward mode. Dust events are characterized by a large turbid layer between 2 and 5 km height while pollution events show a lower vertical development with a thick layer below 3 km in altitude. However low level dust transport is also reported during spring while aerosol pollution layer between 2 and 4 km height has been also observed. We report an effective lidar ratio at 355 nm for pollution aerosols 68 (±13) Sr while it is 63 (±18) Sr for dust. The daily mean AOD at 355 nm for dust events is 0.61 (±0.14) and 0.71 (±0.16) for pollution aerosols events.

1 Introduction

The Mediterranean area has been identified as a “hot-spot” in terms of vulnerability to climate change (Giorgi, 2006). The hydrological cycle of the basin is particularly vulnerable to global warming, showing a 20 % decrease in the availability of land surface water and a 24 % increase in the loss of fresh water over the Mediterranean sea due

ACPD
15, 9507–9540, 2015

to precipitation reduction and warming-enhanced evaporation (Mariotti et al., 2008). It has been recognized that tropospheric aerosol interact significantly on the climate system and the hydrological cycle (Le Treut, 1999; Ramanathan et al., 2001a). Moreover the type and abundance of atmospheric aerosols is one of the key issue regarding regional climate change over the Mediterranean (Nabat et al., 2015). Indeed aerosols scatter and absorb solar light and thermal radiation and thus perturb the radiative balance (e.g. Forster et al., 2007). Aerosols also interact with the water cycle because they act as cloud condensation nuclei (e.g. Rosenfeld et al., 2001). Moreover, they can also significantly impact the vertical stability of the atmosphere by modifying the heating rate profile and reducing the solar irradiance at the surface (Ramanathan et al., 2001b). Because of their short lifetime in the atmosphere compared to greenhouse gases, their radiative impact has a pronounced regional pattern (e.g. Le Treut et al., 1998). In the Mediterranean region, such variability has been shown to have significant effects on the variability in surface radiation and consequently on sea surface evaporation and climate variability (Nabat et al., 2014, 2015). The aerosol concentration, types and optical properties are highly variable over the Mediterranean because of the large diversity in the sources, which are both from natural and anthropogenic origins. The vertical distribution is also complex and often shows several layers with different types of particles. The marine boundary layer is under the influence of primary and secondary marine aerosols and anthropogenic emissions from major coastal urban or industrial areas. The free troposphere above the basin is often affected by the transport of mineral dust from North Africa (Papayannis et al., 2009) and occasionaly by biomass burning aerosols from Europe (Balis et al., 2003) and North America (Formenti et al., 2002). Many studies based on lidar soundings have been dedicated to the characterization of the aerosol vertical distribution over the Mediterranean (Hamonou et al., 1999; Gobbi et al., 2000, 2015; di Sarra et al., 2001; Tomasi et al., 2003; Dulac and Chazette, 2003; Waquet et al., 2005; Balis et al., 2003; Papayannis et al., 2009; Berthier et al., 2006). Those studies show that the transport of mineral dust from North Africa has a significant impact on the vertical distribution of aerosols in the Mediter-

ACPD
15, 9507–9540, 2015

ranean region (e.g., Matthias et al., 2004; di Iorio et al., 2009). Over Lampedusa Island (35.5° N, 12.6° E) di Iorio et al. (2009) have shown that the maximum of altitude of desert dust reaches 8 km in spring while non-desert dust aerosols are confined below 4 km. Such high altitude has been also observed over Potenza (40.6° N, 15.7° E) by Mona et al. (2006). Amiridis et al. (2005) report lower altitude at about 6 km over Thessaloníki (40.5° N, 22.9° E) as well as Pérez et al. (2004) and Waquet et al. (2005) in the western basin.

In this paper, we focus on the northern part of the western basin. As shown by satellite analysis (Barnaba and Gobbi, 2004; Antoine and Nobileau, 2004) this area is on average at the northern bound of the desert dust influence zone while it is also directly affected by the emissions of the large industrial and urban areas of southern France, eastern Spain and northern Italy. We present in this paper the observations on aerosol vertical profiles performed in Corsica Island from 2011 to 2013 using a backscatter lidar located in the north of the island. The northern tip of Corsica has already been identified as an adequate location for atmospheric chemistry measurements (Lambert et al., 2011). The system was operated continuously from February 2011 to April 2011 and from February 2012 up to August 2013. The lidar data are analyzed together with concurrent sun photometer and satellite data that are presented in the next section. We present the methods used for retrieving the profile of aerosol extinction coefficient from lidar signal and we analyse the time series of aerosol layer altitude and optical properties. Significant events in terms of their contribution to the total aerosol depth are then discussed.

2 Aerosol optical depth from sun photometer and satellite

An automated CIMEL-318 sun photometer (Holben et al., 1998) was set up for the first time in June 2008 in Ersa (43.0° N, 9.35° E). However due to large gap in the data during the lidar operation period, we didn't use this database in the present paper. Another sun photometer has been set up on 14 July 2012 in the outskirt of Bastia (42.67° N,

ACPD
15, 9507–9540, 2015

9.43° E), a town of approx. 50 000 inhabitants. The sun photometer measured the direct sun irradiance in spectral channels at 440, 675, 860, 1020 nm at 15 min intervals. A channel at 940 nm is used to retrieve the water vapor columnar content. We have used in this study the level 1.5 aerosol optical depth (AOD) delivered by the version 2 of the direct sun algorithm of the AERONET project. The AOD is extrapolated to 355 nm from measurements at 440 and 675 nm using a power law (Ångström, 1961).

There is a remaining gap in the sun photometer time series in spring 2012. To fill this gap we have collected the AOD retrieved from the Spinning Enhanced Visible and Infrared Imager (SEVIRI) aboard Meteosat Second Generation geostationnary satellite. SEVIRI measures radiances in three spectral solar channels useful for aerosol study (0.6, 0.8 and 1.6 µm) every 15 min with a spatial resolution of 3 km at nadir. The physical background and validation of the algorithm for the AOD and Ångström exponent retrieval is described in Thieuleux et al. (2005). The AOD at 550 nm and the Ångström exponent maps can be downloaded from the ICARE center database (http://www.icare.univ-lille1.fr). The aerosol parameters are retrieved only over the sea and for cloud free pixels. We have selected and averaged all the pixels within a range of 25 km from the lidar site for each of the 15 min slots. The AOD at 355 nm is extrapolated from 550 nm by using a power law and the corresponding Ångström coefficient. The hourly average AOD is computed for hours with at least 2 observations.

We have performed a validation of the SEVIRI AOD by comparing the hourly mean SEVIRI AOD to the AOD measured by the sun photometer in Bastia from July 2012 to August 2013 corresponding to a total of 1574 data. Figure 1 shows that the extrapolated AOD fits very well the sun photometer measured ones with a correlation coefficient of $R = 0.91$. The intercept of 0.01 is within the error generaly admitted for the sun photometer AOD. The slope (0.97 ± 0.01) indicates a slight underestimation of the satellite retrieved AOD that could be due to the fact that the photometer is situated inland in a peri-urban area whereas SEVIRI marine pixels are several km off from the coast.

ACPD
15, 9507–9540, 2015

Figure 2 shows the time series of the daily mean SEVIRI AOD and derived Ångström exponent from February 2011 to August 2013. AOD at 550 nm ranges between 0.05 and 0.8 and Ångström exponent between 0.04 and 1.78 respectively. The AOD remains close to 0.1 from October to March while during spring and summer we observe a much higher variability. 90 % of the daily mean AOD remains below 0.26. The times series indicate that the atmosphere over Corsica Island is hardly affected by turbid events with large AOD.

3 Lidar observations

We performed in situ soundings with a Rayleigh–Mie backscatter lidar ALS 300 manufactured by Leosphere (Lolli et al., 2008). The lidar uses a tripled, pulsed Nd : YAG laser source at 355 nm with an output energy of 16 mJ and a pulse repetition of 20 Hz.

The time acquisition for each profile is about 1 min, corresponding to an average of 1000 shots. The raw signals are range-corrected. The sky background signal is estimated in the far field and subtracted to the raw signal. The correcting overlap factor for short-range heights where the field of view of the telescope does not overlap the laser beam is estimated from a series of horizontal shots when the atmosphere is stable. This factor is over 0.8 at 120 m above the telescope and close to 1 at 360 m. The lidar was tilted by a zenith angle of 15° to the North so the step in altitude is 14.5 m. We consider only the altitude levels above 145 m a.s.l. The lidar was set up for the first time from 15 February to 14 April 2011 at the sun photometer site in Bastia. It was reinstalled at the same place on 15 February 2012 and was operating until 28 August 2013. The lidar was moved 50 km southward in San-Giuliano (42.28° N, 9.51° E) from the 22 June to the 11 July 2012. This dataset is included in the present study. The overall data base contains more than 170 000 profiles. In the following, we consider only hourly average, leading to about 14 000 h of observations.

ACPD
15, 9507–9540, 2015

3.1 Cloud screening

The aerosol extinction coefficient is not retrieved in case of clouds below the reference level. Indeed, clouds will drastically decrease the signal-to-noise ratio or even prevent the laser beam to reach clear air. The retrieval of aerosol extinction coefficient requires avoiding any contamination of the profiles by low clouds. Low clouds can be detected in the lidar profiles because they are associated with a sharp increase in the return signal that is highly variable from one shot to the other. The cloudy profiles are automatically detected using a simple procedure commonly used in satellite image processing (Coakley and Bretherton, 1982; Moulin et al., 1997). We select a set of 3 consecutive profiles over a period of 24 h. The profiles are standardized. For each altitude and each set of 3 consecutive hourly profiles we compute the 3×3 neighborhood mean and standard deviation. Cloudy structures have an abnormal mean and standard deviation. We retain a threshold of 1.0 for the mean and 0.5 for the standard deviation, i.e. above such thresholds the profile is flagged as cloudy. Figure 3 is an example of cloud masking obtained between 24 and 27 May 2012. Gray areas correspond to the cloud mask. During this period, all the clouds between 2 and 6 km are detected (Fig. 3a) and the corresponding contaminated profiles are automatically discarded (Fig. 3b).

Such a procedure removes 52 % of the total number of the 14 370 hourly acquired profiles. On a monthly basis, the screening ranges between a minimum of 26 % of cloudy data in August 2012 to a maximum of 72 % in March 2013.

3.2 Extinction coefficient

The aerosol extinction coefficient is retrieved from the range-corrected attenuated backscattering signal following the Klett's method (Klett, 1981; Fernald, 1984; Ansmann and Müller, 2005) and considering both molecules and aerosols. The calibration of the lidar profiles is given as the initial condition used for solving the differential form of the lidar equation for the range corrected signal $S(R)$. The solution for the aerosol

ACPD
15, 9507–9540, 2015

backscattering coefficient β_a is

$$\beta_a(R) + \beta_m(R) = \frac{S(R)\exp\left[-2\int_{R_0}^{R}[L_a(r) - L_m]\beta_m(r)\,dr\right]}{S^*(R_0) - 2\int_{R_0}^{R} L_a(r)\,S(r)\,T(r,R_0)\,dr} \quad (1)$$

where β_m is molecular backscattering coefficient, and

$$T(r,R_0) = \exp\left[-2\int_{R_0}^{r}[L_a(r') - L_m(r')]\beta_m(r')\,dr'\right]. \quad (2)$$

where L_a and L_m are the particulate and molecular lidar ratio, respectively. The extinction coefficient is given by

$$\alpha_a(R) = \beta_a(R)\cdot L_a(R) \quad (3)$$

The initial condition $S^*(R_0)$ (Eq. 4) is taken in the far range R_0 and above 7 km height where the aerosol contribution is negligible compared to the molecular one.

$$S^*(R_0) = \frac{S(R_0)}{\beta_a(R_0) + \beta_m(R_0)} \quad (4)$$

The choice of an adequate aerosol lidar ratio (ratio of aerosol extinction to backscattering coefficient) is a key issue in the analysis of single wavelength backscattering lidar data. This parameter may vary between 27 Sr for maritime aerosol and 71 Sr for urban/industrial pollution at 550 nm (Cattrall et al., 2005). The lidar ratio is a function of the altitude as it depends on the vertical stratification of the atmosphere, and on the aerosol optical properties transported in the different layers, their hygroscopicity, and the profile of relative humidity. In case of a single wavelength backscattering lidar, we can't derive any information on the vertical variability of this parameter so the lidar

ACPD
15, 9507–9540, 2015

ratio is first assumed to be constant as a function of the altitude. The AOD is used as a constrain for the lidar ratio selection in the extinction retrieval (Chazette, 2003; Léon et al., 2009). Different values of $L_a(R)$ are tested until the vertical integration of $\alpha_a(R)$ (Eq. 3) is equal to the sun photomoter AOD. When no AOD value is available (nighttime or clouds) we use the same $L_a(R)$ as the previous retrieval. It means that during nighttime, the extinction profiles are retrieved using the $L_a(R)$ given by the lastest inversion on the preceding day. Post-processing of daily mean AOD indicates that AOD above 1.2 corresponds to remaining cloud contamination and so the lidar extinction coefficient profiles are removed from the data set.

The fix lidar ratio retrieved when constraining the retrieval of the hourly extinction profiles with the satellite AOD ranges between 22 and 108 Sr with an average value of 54 ± 23 Sr. This estimation is made over the 1836 h of simultaneous satellite and lidar observations during daytime. There is a slight increase in the lidar ratio as a function of the AOD. Considering AOD below 0.05 the average lidar ratio is 42 Sr while it is 62 Sr in high aerosol condition, i.e. when AOD is above 0.5.

Figure 4 presents the comparison between sun photometer, lidar and satellite AOD at 355 nm on a monthly basis. There is an excellent consistency for the months were all the measurements are available. A seasonal cycle is clearly observed with minima in winter and maxima in spring–summer. Local maxima are observed in July 2012 (0.4), July 2013 (0.44) and in March 2012 (0.28). However no clear maximum is observed in spring 2013.

The monthly mean aerosol extinction profiles (Fig. 5) shows a weak variability. The extinction coefficient tends to increase above 4 km from April to June and in September which probably corresponds to the overpass of dust events. The extinction coefficient below 2 km is maximum from June to September which correponds in majority to the period of polluted photochemical or smoke aerosol events.

ACPD
15, 9507–9540, 2015

3.3 Comparison with ground-level data

A TSI 3-wavelength integrating nephelometer was operated at the Ersa station (43.0° N, 9.35° E, 530 m a.s.l.) since May 2012. The nephelometer is located 37 km away from the lidar on a North–South axis. The pseudo-total backscattering (integration of the scattering function for scattering angles between 7and 170°) is measured at 450, 550 and 700 nm. The error due to the truncation in the phase function is corrected following Anderson and Ogren (1998). The aerosol scattering coefficient is extrapolated to 355 nm from the measurements at 450 and 550 nm following the Ångström law.

Figure 6 shows the comparison between the daily mean total aerosol scattering coefficient derived from the integrating nephelometer and the mean aerosol extinction coefficient between 450 and 550 m a.s.l. derived from the lidar. The extinction coefficient is the sum of the scattering and absorption coefficient and so it has to be higher or egal to the scattering coefficient. Since the measurement sites are not collocated it is not possible to estimate the single scattering albedo, that is the ratio between scattering and extinction coefficient. However we have a similar trend showing low scattering, respectively extinction coefficient during winter period and a maximum value in July 2013. When considering the coincident data the correlation coefficient is 0.63 (N = 302 data).

3.4 Layer altitude

The variation in the aerosol concentration and optical properties between the different layer induces gradients in the attenuated range corrected lidar signal. In the lower part of the atmosphere where the signal to noise ratio is the higher, we classify at least two layers using the second derivative of the lidar signal (Menut et al., 1999). In the upper part of the atmosphere where the gradients and the signal to noise ratio are smaller the derivative of the signal doesn't lead a clear detection of the dust layer. As an indicator of the vertical development of the aerosol layer, we compute the AOD scale height, i.e.

ACPD
15, 9507–9540, 2015

the altitude at which $1/e$ of the total AOD is below that point (Turner et al., 2001; Léon et al., 2009).

We detect a shallow marine boundary layer on most of the profiles. The average altitude is 380 ± 260 m. A weak seasonal cycle is observed with a summer maximum at 460 m in July and a winter minimum at 250 m in December. The daytime variability is also lower during winter months (November to March). We also detect a secondary maximum in the derivative of the lidar signal located between 700 m and 3.5 km and on average at 1.3 ± 0.5 km. This secondary gradient in the lidar signal can be due to the complex local atmospheric circulation because of the proximity of both the sea shore and the high topography of the island. The mean scale height is 4.1 ± 1.6 km. The scale height reaches 5 km during the dust outbreak in March 2013. Below the scale height the mean hourly aerosol extinction coefficient is $0.07 \pm 0.17\,\mathrm{km}^{-1}$. It is $0.05 \pm 0.08\,\mathrm{km}^{-1}$ in the marine boundary layer.

3.5 Synthesis

The two main phenomena leading to strong AODs over Corsica are dust outbreaks from Northern Africa and advection of pollution or biomass burning from Europe. The AOD at 550 nm and the Ångström coefficient are used to classify 3 types of aerosol conditions: maritime, dust and pollution aerosols. Maritime situations correspond to AOD below 0.3 (Barnaba and Gobbi, 2004) whatever values of the Ångström coefficient. Pollution aerosol conditions are identified with AOD above 0.3 and Ångström coefficient above 1.2 while dust cases correspond to AOD above 0.3 and Ångström coefficient below 0.9 (Hamonou et al., 1999). From February 2012 to August 2013, only 28 out of 341 days of observation have an AOD above 0.3, i.e. 8 % of the observations. Among those 28 days, 43 % (12 days) are identified as dust and 32 % (9 days) as pollution events.

In Table 1 we give the daily average aerosol properties according to the previous classification. Low AOD denomination corresponds to maritime situation for which the AOD at 550 nm is below 0.1. The average AOD at 550 nm is higher for the dust than

ACPD
15, 9507–9540, 2015

for the pollution cases. However because of the high Ångström exponent for polluted fine particles, it is the opposite at 355 nm. Considering cases with a low AOD, the Ångström exponent is 0.52 indicating a main contribution of large sea salt particles. The lidar ratio at 355 nm for those cases is 49 Sr. The effective lidar ratio found for dust is 63 (±18) Sr. This value is higher than the one retrieved by Müller et al. (2007) but in the range of previously published values in the Mediterranean (Balis et al., 2004). However, in our case the lidar ratio is not vertically resolved and thus is biased by the contribution of marine and pollution aerosols in the marine boundary layer. In the case of the long range transport of pollution aerosols which occurs at a lower altitude as it is shown by the lower scale height, the lidar ratio of 69 Sr is more reliable and in a better agreement with previously published values (Ackermann, 1998). The high scale height for low AOD is due to the weak contribution of the clean boundary layer to the total AOD. The difference in the altitude of the transport for dust and pollution aerosols is highlighted by a higher scale height for dust than for pollution particles. In the next section, we focus on this difference by analyzing selected case studies.

4 Discussion on specific events

4.1 Analysis of satellite data

Figure 7 shows the daily mean AOD over the western Mediterranean basin during the dust events which affected Cap Corse during 2012–2013 period. The major dust event in terms of AOD occurred in April–May 2013 (Fig. 7d) with a paroxysm on 30 April when the AOD reached 0.89 (daily mean at 355 nm). SEVIRI Ångström exponent is 0.27 indicating a large contribution of coarse particles to the AOD. Such corridor is a well known feature of the dust transport in the Mediterranean (Hamonou et al., 1999) and forms when low-pressure systems enter the northwestern part of the basin (Gkikas et al., 2012) in spring or autumn (Waquet et al., 2005). The dust storm is associated with clouds that prevent from retrieving AOD over large parts of the plume and lead

ACPD
15, 9507–9540, 2015

to a patchy structure when averaging during the whole dust event between 30 April to 4 May 2012. The second dust event in magnitude observed over the site occurred in June–July 2012 (Fig. 7b) with a SEVIRI AOD at 0.8 on 30 June 2012 (Nabat et al., 2014). In this case the advection pattern is different. The saharan air layer advected over north-east Atlantic and western Spain during the dust event is recirculated to the northwestern part of the basin by westerly winds. A larger SEVIRI Ångström exponent of 0.6 is observed for this dust outbreak which can be linked to a smaller contribution of large particles to the AOD than in the case of spring event. A similar pattern is observed for the 19 June 2012 (Fig. 7a). Finally, the Fig. 7d shows the case of a dust storm in the western basin on July 2012 where the core of the dust plume doesn't reach the Cap Corse and the gulf of Genova so the AOD remains rather weak in this area.

The highest pollution event observed occurred on July 2013. Figure 8d shows the mean daily SEVIRI AOD between 13–20 July 2013. The SEVIRI AOD reached 0.53 (daily mean) on 14 July and increased to 0.6 on 15 July. The Ångström exponent is 1.33 so leading to an AOD of 0.95 at 355 nm on 14 July 2013. During this period, the pollution plume is observed all along the northern coast of the basin including the Balearic islands and Corsica (Fig. 8d) while a local maximum at 0.4 is observed in the gulf of Genova. A rather similar case was observed on 6 September 2012 (Fig. 8c). However the plume is limited to the gulf of Genova. The geographic position of the low pressure system in the northern basin affects the extent of the plume. In this case the low is located in the gulf of Genova, while in July 2013 it is located westward over Spain. The second major pollution event in term of AOD occurs on 26 March 2012. SEVIRI observations indicate a large plume crossing the northern part of the western basin (Fig. 8a). The corresponding daily mean AOD at 355 nm is 0.75 and the Ångström exponent is 1.25. This moderate value tends to indicate a possible contribution of large particles. In this case the low is southward over Sicily bringing more continental air from central Europe to the basin. The case of August 2012 (Fig. 8b) is ambiguous because despite an Ångström exponent of 1.3 the satellite pictures indicates a possible contribution of dust particles from northern Africa.

ACPD
15, 9507–9540, 2015

4.2 Vertical profiles and air mass origin

We further analyze the stratification of the aerosol layers and their possible origin and transport pathway. The air mass origins for the aforementioned specific events are analyzed using the Lagrangian particle dispersion model FLEXPART (Stohl et al., 1998). The model is run in backward mode (Seibert and Frank, 2004) over 10 days. The meteorological forcing is given by ECMWF operational analysis at 0.5°. The plume is computed using 1 000 000 particles released for a given range of altitudes and arriving in 1° × 1° box centered on the Cap Corse station. The ranges of altitudes are selected to highlight some particular features of the aloft aerosol transport. The residence time is computed for the whole duration of the simulation and integrated between the surface level and the top altitude of the release. The retroplume residence times (in seconds) gives the density of probability of the origin of the air mass that arrived at the station in the given altitude range from below altitudes.

Figure 9 presents the vertical profiles of the aerosol extinction coefficient obtained during the aforementioned events. Lidar data were not available on 19 June 2012. Figure 9a to 9e is for dust events and Fig. 9f to 9i is for pollution events. The main feature corresponding to the pollution cases profiles is the low level of altitude in the transport of aerosols. The 26 March 2012 (Fig. 9f) and 6 September 2012 (Fig. 9h) are very similar in terms of vertical distribution showing a thick layer between 1 and 3 km height. The backward simulations of the air masses arriving at the station between 500 and 2000 m a.s.l. (Fig. 10a and b) indicates a most probable transport from Eastern Europe. The aerosol extinction coefficient in the pollution layer reached 0.15 and 0.25 km^{-1} on 26 March and 6 September 2012, respectively. The value of extinction coefficient encountered during those events might be explained by the advection of air masses contaminated by biomass burning by-products originating from southeast Europe. Indeed for both events, Global Fire Assimilation System (Kaiser et al., 2012) biomass burning emission inventory shows biomass burning emissions on the pathways of air masses arriving to the Cap Corse (not shown here).

ACPD
15, 9507–9540, 2015

The case of summer 2012 (Fig. 9g) and summer 2013 shows additional elevated layers. The extinction coefficient below 700 m increased from 0.09 to 0.19 km^{-1} from 20 to 25 August 2012 showing the build up of the pollution event during this period. Below 2 km height, the air mass was originating from the gulf of Genova and coastal areas of Italy. The aerosol layer observed between 2.5 and 4 km height was originating from Spain and Southern France (Fig. 10c) and passed over the Pyrenees mountain range. The backward plume shows also a possible northwestern African origin and thus possibly carrying dust that might explains the rather low value for the Ångström exponent.

During the month of July 2013 we observed a large increase in the AOD (Fig. 2). This increase was also well observed in the aerosol scattering coefficient measured at the Ersa station (Fig. 6). Below 1 km the aerosols are originating from the Pô valley (northern Italy) and we observed a large variability in the extinction coefficient ranging between 0.1 on the 15 July (9i, black solid line) and almost 0.2 km^{-1} (9g, red solid line) on the 19 July. A large aerosol layer was observed aloft between 2 and 4 km height (Fig. 9i). The air mass backtrajectory (Fig. 10d) indicated that the air mass was originating from northern Europe and underwent an ascent over the Alps before arriving above Cap Corse. An additional aerosol layers was also observed between 1 and 2 km height during the pollution event.

The dust events observed during summer 2012 (Fig. 9a and b) are rather similar in terms of vertical distribution. We observed a thick dust layer with a top located at 5 km height. The maximum extinction coefficient in the dust layer is 0.12 km^{-1}. The bottom of the layer is located between 2 and 3 km. The air mass origin simulations indicate a transport of dust from North western Africa. In late June (Figs. 9a and 10e) the plume is first advected over the Atlantic and then transported to the east over the strait of Gibraltar. While the dust case in July (Fig. 9b) shows an advection of the plume east of the coast of Spain (Fig. 10f). The event observed in July 2013 (Fig. 9d) has a lower extinction coefficient at 0.06 km^{-1} but with a similar vertical structure than the previous cases. The advection pattern of the dust (not shown) was the same as for

ACPD
15, 9507–9540, 2015

the case in June 2012. On August 2013 (Fig. 9e) the profile shows a dust layer up to 7 km. The extinction coefficient is 0.1 km^{-1} however such a high altitude event has an impact on the estimation of the extinction coefficient as the reference zone is affected by aerosols. The air mass backward simulations show the advection of the dust from the northwestern Sahara with an ascent over the Atlas mountain range (Fig. 10g).

A large dust layer arrived on the 30 April (Fig. 9c, black solid line) between 1 and 4 km height with extinction coefficient over 0.3 km^{-1}. To highlight the variability in the aerosol vertical distribution during the dust event in April–May 2013 (Fig. 9c) we plotted the aerosol extinction on the 30 April and the 2 May. As the dust event passed over the site (Fig. 9c, red solid line), we observed an increase in the extinction coefficient below 2 km while the aloft layer vanished. Figure 10h highlights an advection pattern that is different to the summer cases. The dust is transported in a southerly flow across northwestern Sahara and then over Tunisia before reaching the station. This kind of synoptic situation favors first the transport in altitude of air masses uplift in northwestern Sahara and then the low level transport of dust from closest sources in southern Tunisia.

5 Conclusions

We present for the first time lidar observations in the north of Corsica Island during more than a year. The combined analysis of satellite and lidar observation shows that the aerosol optical depth in the northern part of the western basin remains moderate most of the time. The AOD has a clear seasonal cycle with minima during winter and maxima in spring and summer. The increase in the AOD is linked to the large scale advection of polluted air masses from Europe or dusty air masses from North Africa. However large AOD events (above 0.3 at 550 nm) represent less than 10 % of the observation days. The average low influence of desert dust events in this area has also been observed by Pey et al. (2013) using ground level PM_{10} mass concentration. For the observed aerosol events the average AOD at 355 nm is 0.61 for dust and 0.71

ACPD
15, 9507–9540, 2015

for pollution aerosols, respectively. The higher AOD for pollution aerosols at 355 nm is associated to a high Ångström exponent, 1.38 compared to 0.60 for dust.

During pollution events, the large increase in the extinction coefficient below 2 km is due to the build up of pollution into the gulf of Genova. We have also observed the transport of polluted air masses above 2 km height either from northern or southwestern Europe and reaching the measurement site after been advected over mountainous areas. Saharan dust transport can be stratified in different layers located between the ground level and up to 7 km height, which is an upper detection limit for the lidar system. The largest dust event in term of AOD is observed during spring and corresponds to a south-north advection of dusty air masses over north-western Africa with an outlet over Tunisia. Other cases are observed in summer and show that the dust is advected to Corsica by westerly winds after being uplifted in Morocco and Algeria and ejected in the western part of the basin.

Our observations corroborate previous studies on the vertical distribution and properties of Mediterranean aerosols (Sicard et al., 2011). The complex stratification of the aerosol transport over the western basin is due to the various origins of the particles, including pollution and biomass burning aerosols from Europe and mineral dust from Northern Africa, and the effect of the topography surrounding the basin. This new dataset obtained in Cap Corse provides a new insight in the vertical distribution of aerosols in the Mediterranean and offers the opportunity to better understand the origin and transport pathways of those particles.

Acknowledgements. The project was supported financially by INSU, ADEME and IRD through MISTRAL/CHARMEX program. The authors want to thank AERONET/PHOTONS team for providing and calibrating the sun photometer. ICARE data center is also acknowledged for providing a free access to SEVIRI aerosol products. The authors thank Qualitair Corse, DREAL Corse and INRA at San-Giuliano for providing local facilities and support. This work is within the frame of CORSICA (Corsican Observatory for Research and Studies on climate and Atmosphere-ocean environment) sponsored by Communauté Territoriale de Corse and FEDER.

ACPD
15, 9507–9540, 2015

References

Ackermann, J.: The extinction-to-backscatter ratio of tropospheric aerosol: a numerical study, J. Atmos. Ocean. Tech., 15, 1043–1050, doi:10.1175/1520-0426(1998)015<1043:TETBRO>2.0.CO;2, 1998. 9518

Amiridis, V., Balis, D. S., Kazadzis, S., Bais, A., Giannakaki, E., Papayannis, A., and Zerefos, C.: Four-year aerosol observations with a Raman lidar at Thessaloniki, Greece, in the framework of European Aerosol Research Lidar Network (EARLINET), J. Geophys. Res., 110, D21203, doi:10.1029/2005JD006190, 2005. 9510

Anderson, T. L. and Ogren, J. A.: Determining aerosol radiative properties using the TSI 3563 integrating nephelometer, Aerosol Sci. Tech., 29, 57–69, doi:10.1080/02786829808965551, 1998. 9516

Ångström, A.: Techniques of determinig the turbidity of the atmosphere, Tellus, 13, 214–223, doi:10.1111/j.2153-3490.1961.tb00078.x, 1961. 9511

Ansmann, A. and Müller, D.: Lidar and atmospheric aerosol particle, in: LIDAR: Range Resolved Optical Remote Sensing of the Atmosphere, edited by: Weitkamp, C., Vol. 102 of Springer Series in Optical Sciences, Springer, Geessthacht, Germany, 105–141, doi:10.1007/0-387-25101-4_4, 2005. 9513

Antoine, D. and Nobileau, D.: Recent increase of Saharan dust transport over the Mediterranean Sea, as revealed from ocean color satellite (SeaWiFS) observations, J. Geophys. Res., 111, D12214, doi:10.1029/2005JD006795, 2004. 9510

Balis, D., Amiridis, V., Zerefos, C., Gerasopoulos, E., Andreae, M. O., Zanis, P., Kazantzidis, A., Kazadzis, S., and Papayannis, A.: Raman lidar and sunphotometric measurements of aerosol optical properties over Thessaloniki, Greece during a biomass burning episode, Atmos. Environ., 37, 4529–4538, doi:10.1016/S1352-2310(03)00581-8, 2003. 9509

Balis, D. S., Amiridis, V., Nickovic, S., Papayannis, A., and Zerefos, C.: Optical properties of Saharan dust layers as detected by a Raman lidar at Thessaloniki, Greece, Geophys. Res. Lett., 31, L13104, doi:10.1029/2004GL019881, 2004. 9518

Barnaba, F. and Gobbi, G. P.: Aerosol seasonal variability over the Mediterranean region and relative impact of maritime, continental and Saharan dust particles over the basin from MODIS data in the year 2001, Atmos. Chem. Phys., 4, 2367–2391, doi:10.5194/acp-4-2367-2004, 2004. 9510, 9517

ACPD
15, 9507–9540, 2015

Berthier, S., Chazette, P., Couvert, P., Pelon, J., Dulac, F., Thieuleux, F., Moulin, C., and Pain, T.: Desert dust aerosol columnar properties over ocean and continental Africa from Lidar in-Space Technology Experiment (LITE) and Meteosat synergy, J. Geophys. Res., 111, D21202, doi:10.1029/2005JD006999, 2006. 9509

Cattrall, C., Reagan, J., Thome, K., and Dubovik, O.: Variability of aerosol and spectral lidar and backscatter and extinction ratios of key aerosol types derived from selected Aerosol Robotic Network locations, J. Geophys. Res., 110, D10S11, doi:10.1029/2004JD005124, 2005. 9514

Chazette, P.: The monsoon aerosol extinction properties at Goa during INDOEX as measured with lidar, J. Geophys. Res., 108, 4187, doi:10.1029/2002JD002074, 2003. 9515

Coakley, J. A. and Bretherton, F. P.: Cloud cover from high-resolution scanner data: detecting and allowing for partially filled fields of view, J. Geophys. Res., 87, 4917–4932, doi:10.1029/JC087iC07p04917, 1982. 9513

di Iorio, T., di Sarra, A., Sferlazzo, D. M., Cacciani, M., Meloni, D., Monteleone, F., Fuà, D., and Fiocco, G.: Seasonal evolution of the tropospheric aerosol vertical profile in the central Mediterranean and role of desert dust, J. Geophys. Res., 114, D02201, doi:10.1029/2008JD010593, 2009. 9510

di Sarra, A., Di Iorio, T., Cacciani, M., Fiocco, G., and Fuà, D.: Saharan dust profiles measured by lidar at Lampedusa, J. Geophys. Res., 106, 10335–10347, doi:10.1029/2000JD900734, 2001. 9509

Dulac, F. and Chazette, P.: Airborne study of a multi-layer aerosol structure in the eastern Mediterranean observed with the airborne polarized lidar ALEX during a STAAARTE campaign (7 June 1997), Atmos. Chem. Phys., 3, 1817–1831, doi:10.5194/acp-3-1817-2003, 2003. 9509

Fernald, F.: Analysis of atmospheric lidar observations: some comments, Appl. Optics, 23, 652–653, doi:10.1364/AO.23.000652, 1984. 9513

Formenti, P., Reiner, T., Sprung, D., Andreae, M. O., Wendisch, M., Wex, H., Kindred, D., Dewey, K., Kent, J., Tzortziou, M., Vasaras, A., and Zerefos, C.: STAAARTE-MED 1998 summer airborne measurements over the Aegean Sea 1. Aerosol particles and trace gases, J. Geophys. Res., 107, 4450, doi:10.1029/2001JD001337, 2002. 9509

Forster, P., Ramaswamy, V., Artaxo, P., Berntsen, T., Betts, R., Fahey, D., Haywood, J., Lean, J., Lowe, D., Myhre, G., Nganga, J., Prinn, R., Raga, G., Schulz, M., and Van Dorland, R.: Changes in atmospheric constituents and in radiative forcing, in: Climate Change 2007: The Physical Basis. Contribution of Working Group I to the Fourth Assessment Report of the

ACPD
15, 9507–9540, 2015

Intergovernmental Panel on Climate Change, edited by: Solomon, S., Qin, D., Manning, M., Chen, Z., Marquis, M., Averyt, K., Tignor, M., and Miller, H., Cambridge University Press, Cambridge, UK and New York, NY, USA, 2007. 9509

Giorgi, F.: Climate change hot-spots, Geophys. Res. Lett., 33, L08707, doi:10.1029/2006GL025734, 2006. 9508

Gkikas, A., Houssos, E., Hatzianastassiou, N., Papadimas, C., and Bartzokas, A.: Synoptic conditions favouring the occurrence of aerosol episodes over the broader Mediterranean basin, Q. J. Roy. Meteor. Soc., 138, 932–949, doi:10.1002/qj.978, 2012. 9518

Gobbi, G., Barnaba, F., Giorgi, R., and Santacasa, A.: Altitude-resolved properties of a Saharan dust event over the Mediterranean, Atmos. Environ., 34, 5119–5127, doi:10.1016/S1352-2310(00)00194-1, 2000. 9509

Gobbi, G. P., Barnaba, F., and Ammannato, L.: The vertical distribution of aerosols, Saharan dust and cirrus clouds in Rome (Italy) in the year 2001, Atmos. Chem. Phys., 4, 351–359, doi:10.5194/acp-4-351-2004, 2004. 9509

Hamonou, E., Chazette, P., Balis, D., Dulac, F., Schneider, X., Galani, E., Ancellet, G., and Papayannis, A.: Characterisation of the vertical structure of Saharan dust export to the Mediterranean bassin, J. Geophys. Res., 104, 22257–22270, doi:10.1029/1999JD900257, 1999. 9509, 9517, 9518

Holben, B., Eck, T., Sluster, I., Tanré, D., Buis, J., Setzer, A., Vermote, E., Reagan, J., Kaufman, Y., Nakajima, T., Lavenu, F., Jankowiak, I., and Smirnov, A.: AERONET-A federated instrument network and data archive for aerosol characterisation, Remote Sens. Environ., 66, 1–16, doi:10.1016/S0034-4257(98)00031-5, 1998. 9510

Kaiser, J. W., Heil, A., Andreae, M. O., Benedetti, A., Chubarova, N., Jones, L., Morcrette, J.-J., Razinger, M., Schultz, M. G., Suttie, M., and van der Werf, G. R.: Biomass burning emissions estimated with a global fire assimilation system based on observed fire radiative power, Biogeosciences, 9, 527–554, doi:10.5194/bg-9-527-2012, 2012. 9520

Klett, J.: Stable analytical inversion solution for processing lidar return signal, Appl. Optics, 20, 211–220, doi:10.1364/AO.20.000211, 1981. 9513

Lambert, D., Mallet, M., Ducrocq, V., Dulac, F., Gheusi, F., and Kalthoff, N.: CORSiCA: a Mediterranean atmospheric and oceanographic observatory in Corsica within the framework of HyMeX and ChArMEx, Adv. Geosci., 26, 125–131, doi:10.5194/adgeo-26-125-2011, 2011. 9510

ACPD
15, 9507–9540, 2015

Léon, J.-F., Derimian, Y., Chiapello, I., Tanré, D., Podvin, T., Chatenet, B., Diallo, A., and Deroo, C.: Aerosol vertical distribution and optical properties over M'Bour (16.96° W; 14.39° N), Senegal from 2006 to 2008, Atmos. Chem. Phys., 9, 9249–9261, doi:10.5194/acp-9-9249-2009, 2009. 9515, 9517

Le Treut, H.: Global hydrological changes associated with a perturbation of the climate system: the role of atmospheric feedbacks, their uncertainty and their validation, Adv. Water Resour., 23, 121–131, doi:10.1016/S0309-1708(99)00016-0, 1999. 9509

Le Treut, H., Forichon, M., Boucher, O., and Li, Z.-X.: Sulfate aerosol indirect effect and CO_2 greenhouse forcing: equilibrium response of the LMD GCM and associated cloud feedbacks, J. Climate, 11, 1673–1684, doi:10.1175/1520-0442(1998)011<1673:SAIEAC>2.0.CO;2, 1998. 9509

Lolli, S., Welton, E., and Sauvage, L.: EZ LIDAR measurement results in the frame of Indian Monsoon TIGER-Z NASA campaign, in: Lidar Technologies, Techniques, and Measurements for Atmospheric Remote Sensing IV, edited by: Singh, U. and Pappalardo, G., vol. Proc. SPIE 7111, p. 71110I, Cardiff, UK, doi:10.1117/12.803720, 2008. 9512

Mariotti, A., Zeng, N., Yoon, J.-H., Artale, V., Navarra, A., Alpert, P., and Li, L. Z.: Mediterranean water cycle changes: transition to drier 21st century conditions in observations and CMIP3 simulations, Environ. Res. Lett., 3, 044001, doi:10.1088/1748-9326/3/4/044001, 2008. 9509

Matthias, V., Balis, D., Bösenberg, J., Eixmann, R., Iarlori, M., Komguem, L., Mattis, I., Papayannis, A., Pappalardo, G., Perrone, M., and Wang, X.: Vertical aerosol distribution over Europe: Statistical analysis of Raman lidar data from 10 European Aerosol Research Lidar Network (EARLINET) stations, J. Geophys. Res., 109, D18201, doi:10.1029/2004JD004638, 2004. 9510

Menut, L., Flamant, C., Pelon, J., and Flamant, P. H.: Urban boundary-layer height determination from lidar measurements over the Paris area, Appl. Optics, 38, 945–954, 1999. 9516

Mona, L., Amodeo, A., Pandolfi, M., and Pappalardo, G.: Saharan dust intrusions in the Mediterranean area: three years of Raman lidar measurements, J. Geophys. Res., 111, D16203, doi:10.1029/2005JD006569, 2006. 9510

Moulin, C., Guillard, F., Dulac, F., and Lambert, C. E.: Long-term daily monitoring of Saharan dust load over ocean using Meteosat ISCCP-B2 data: 1. Methodology and preliminary results for 1983–1994 in the Mediterranean, J. Geophys. Res., 102, 16947–16958, doi:10.1029/96JD02620, 1997. 9513

ACPD
15, 9507–9540, 2015

Müller, D., Ansmann, A., Mattis, I., Tesche, M., Wandinger, U., Althausen, D., and Pisani, G.: Aerosol-type-dependent lidar ratios observed with Raman lidar, J. Geophys. Res., 112, D16202, doi:10.1029/2006JD008292, 2007. 9518

Nabat, P., Somot, S., Mallet, M., Michou, M., Sevault, F., Driouech, F., Meloni, D., Di Sarra, A., Di Biagio, C., Formenti, P., Sicard, M., Léon, J.-F., and Bouin, M.-N.: Dust aerosol radiative effects during summer 2012 simulated with a coupled regional aerosol–atmosphere–ocean model over the Mediterranean, Atmos. Chem. Phys. Discuss., 14, 25351–25410, doi:10.5194/acpd-14-25351-2014, 2014. 9509, 9519

Nabat, P., Somot, S., Mallet, M., Sevault, F., Chiacchio, M., and Wild, M.: Direct and semi-direct aerosol radiative effect on the Mediterranean climate variability using a coupled regional climate system model, Clim. Dynam., 44, 1127–1155, doi:10.1007/s00382-014-2205-6, 2015. 9509

Papayannis, A., Mamouri, R. E., Amiridis, V., Kazadzis, S., Pérez, C., Tsaknakis, G., Kokkalis, P., and Baldasano, J. M.: Systematic lidar observations of Saharan dust layers over Athens, Greece in the frame of EARLINET project (2004–2006), Ann. Geophys., 27, 3611–3620, doi:10.5194/angeo-27-3611-2009, 2009. 9509

Pérez, C., Sicard, M., Jorba, O., Comerón, A., and Baldasano, J. M.: Summertime recirculations of air pollutants over the north-eastern Iberian coast observed from systematic EARLINET lidar measurements in Barcelona, Atmos. Environ., 38, 3983–4000, doi:10.1016/j.atmosenv.2004.04.010, 2004. 9510

Pey, J., Querol, X., Alastuey, A., Forastiere, F., and Stafoggia, M.: African dust outbreaks over the Mediterranean Basin during 2001–2011: PM_{10} concentrations, phenomenology and trends, and its relation with synoptic and mesoscale meteorology, Atmos. Chem. Phys., 13, 1395–1410, doi:10.5194/acp-13-1395-2013, 2013. 9522

Ramanathan, V., Crutzen, P. J., Kiehl, J. T., and Rosenfeld, D.: Aerosols, climate, and the hydrological cycle, Science, 294, 2119–2124, doi:10.1126/science.1064034, 2001a. 9509

Ramanathan, V., Crutzen, P. J., Lelieveld, J., Mitra, A. P., Althausen, D., Anderson, J., Andreae, M. O., Cantrell, W., Cass, G. R., Chung, C. E., Clarke, A. D., Coakley, J. A., Collins, W. D., Conant, W. C., Dulac, F., Heintzenberg, J., Heymsfield, A. J., Holben, B., Howell, S., Hudson, J., Jayaraman, A., Kiehl, J. T., Krishnamurti, T. N., Lubin, D., McFarquhar, G., Novakov, T., Ogren, J. A., Podgorny, I. A., Prather, K., Priestley, K., Prospero, J. M., Quinn, P. K., Rajeev, K., Rasch, P., Rupert, S., Sadourny, R., Satheesh, S. K., Shaw, G. E., Sheridan, P., and Valero, F. P. J.: Indian Ocean Experiment: an integrated analysis of the cli-

ACPD
15, 9507–9540, 2015

mate forcing and effects of the great Indo-Asian haze, J. Geophys. Res., 106, 28371–28398, doi:10.1029/2001JD900133, 2001b. 9509
Rosenfeld, D., Rudich, Y., and Lahav, R.: Desert dust suppressing precipitation: a possible desertification feedback loop, P. Natl. Acad. Sci. USA, 98, 5975–5980, doi:10.1073/pnas.101122798, 2001. 9509
Seibert, P. and Frank, A.: Source-receptor matrix calculation with a Lagrangian particle dispersion model in backward mode, Atmos. Chem. Phys., 4, 51–63, doi:10.5194/acp-4-51-2004, 2004. 9520
Sicard, M., Rocadenbosch, F., Reba, M. N. M., Comerón, A., Tomás, S., García-Vízcaino, D., Batet, O., Barrios, R., Kumar, D., and Baldasano, J. M.: Seasonal variability of aerosol optical properties observed by means of a Raman lidar at an EARLINET site over Northeastern Spain, Atmos. Chem. Phys., 11, 175–190, doi:10.5194/acp-11-175-2011, 2011. 9523
Stohl, A., Hittenberger, M., and Wotawa, G.: Validation of the Lagrangian particle dispersion model FLEXPART against large-scale tracer experiment data, Atmos. Environ., 32, 4245–4264, doi:10.1016/S1352-2310(98)00184-8, 1998. 9520
Thieuleux, F., Moulin, C., Bréon, F. M., Maignan, F., Poitou, J., and Tanré, D.: Remote sensing of aerosols over the oceans using MSG/SEVIRI imagery, Ann. Geophys., 23, 3561–3568, doi:10.5194/angeo-23-3561-2005, 2005. 9511
Tomasi, F. D., Blanco, A., and Perrone, M. R.: Raman lidar monitoring of extinction and backscattering of African dust layers and dust characterization, Appl. Optics, 42, 1699–1709, doi:10.1364/AO.42.001699, 2003. 9509
Turner, D. D., Ferrare, R. A., and Brasseur, L. A.: Average aerosol extinction and water vapor profiles over the Southern Great Plains, Geophys. Res. Lett., 28, 4441–4444, doi:10.1029/2001GL013691, 2001. 9517
Waquet, F., Léon, J.-F., Goloub, P., Pelon, J., Tanré, D., and Deuzé, J.-L.: Maritime and dust aerosol retrieval from polarized and multispectral active and passive sensors, J. Geophys. Res., 110, D10S10, doi:10.1029/2004JD004839, 2005. 9509, 9510, 9518

ACPD
15, 9507–9540, 2015

Table 1. Mean aerosol optical depth (AOD) at 355 and 550 nm, Ångström exponent, lidar ratio at 355 nm and scale height.

	AOD 550 nm (–)	AOD 355 nm (–)	Ang. Exp. (–)	Lr 355 nm (Sr)	H (km)
Total	0.16 (±0.09)	0.25 (±0.16)	0.88 (±0.41)	55 (±21)	3.9 (±1.0)
Dust	0.47 (±0.13)	0.61 (±0.14)	0.60 (±0.17)	63 (±18)	4.0 (±0.8)
Anthrop.	0.39 (±0.09)	0.71 (±0.16)	1.38 (±0.09)	68 (±13)	3.2 (±0.6)
low AOD	0.08 (±0.01)	0.10 (±0.01)	0.52 (±0.27)	49 (±20)	4.6 (±0.7)

ACPD
15, 9507–9540, 2015

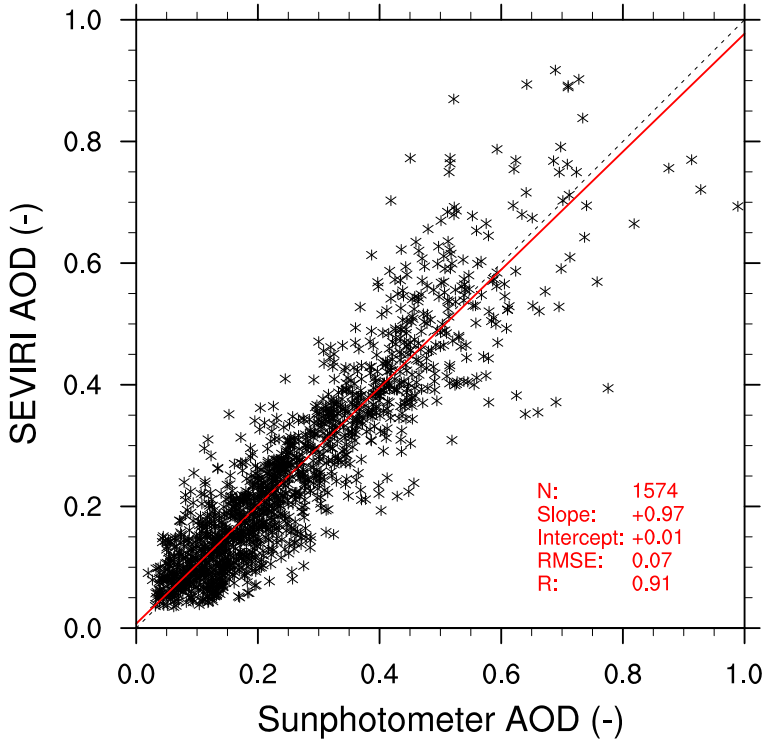

Figure 1. Comparison between sun photometer and SEVIRI AOD. The wavelength is 355 nm.

ACPD
15, 9507–9540, 2015

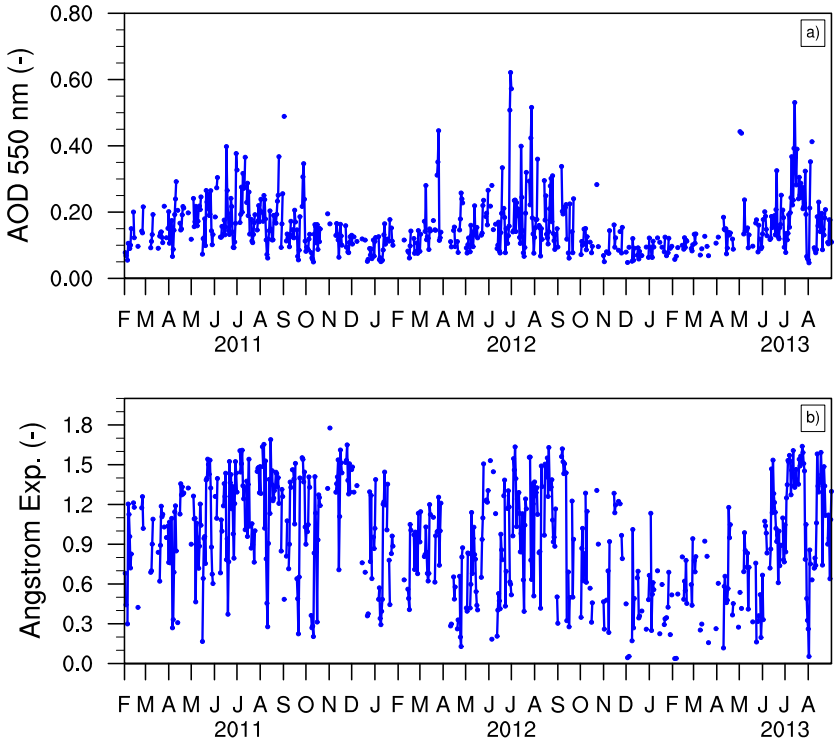

Figure 2. SEVIRI daily mean **(a)** aerosol optical depth and **(b)** Ångström exponent close to the lidar site.

ACPD
15, 9507–9540, 2015

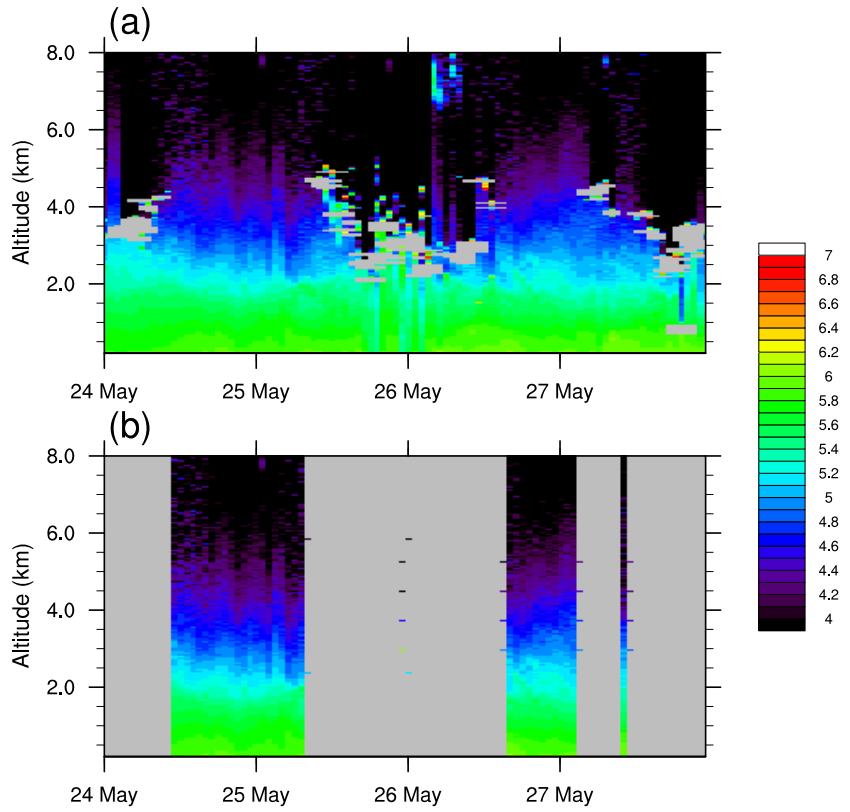

Figure 3. Time series of the range corrected lidar signal between 24 and 27 May 2012. **(a)** Low level clouds and **(b)** corresponding profiles are shaded in gray.

ACPD
15, 9507–9540, 2015

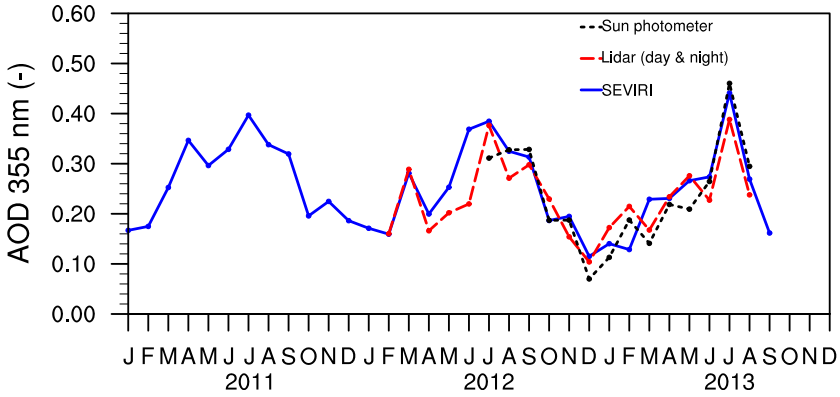

Figure 4. Monthly mean AOD at 355 nm for the lidar (averaged during day and night), Sun photometer and SEVIRI (only daytime) from January 2011 to December 2013.

ACPD
15, 9507–9540, 2015

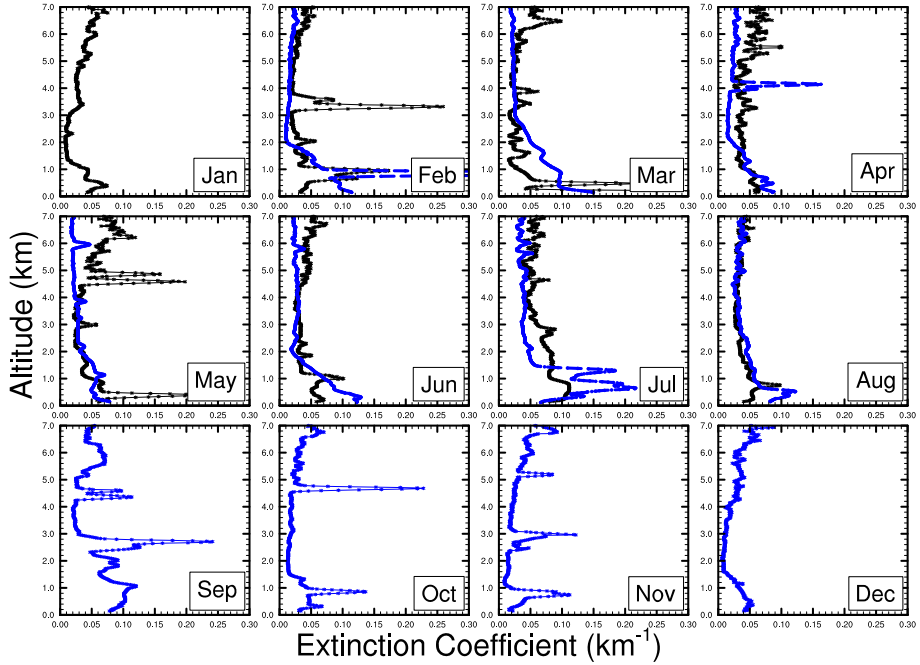

Figure 5. Monthly mean aerosol extinction profiles at 355 nm for (blue) 2012 and (black) 2013.

ACPD
15, 9507–9540, 2015

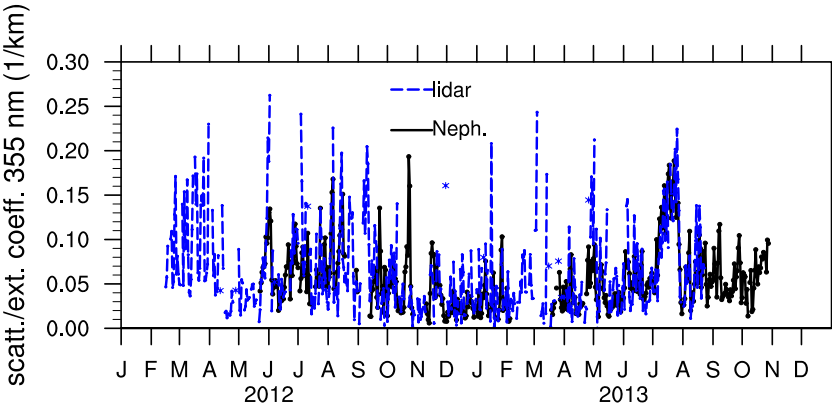

Figure 6. Nephelometer total scattering coefficient at Ersa station and mean extinction coefficient between 450 and 550 m a.s.l. derived from the lidar.

ACPD
15, 9507–9540, 2015

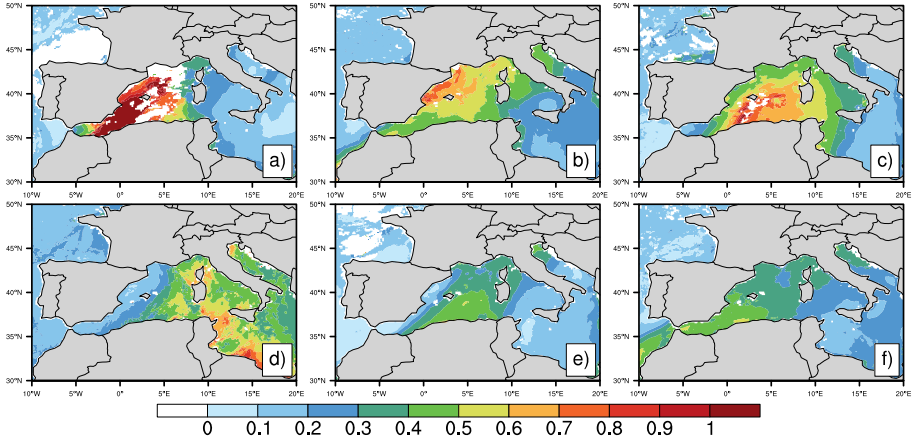

Figure 7. Mean daily SEVIRI AOD at 550 nm corresponding to identified dust episodes at Cap Corse **(a)** for 19 June 2012, **(b)** from 29 June to 1 July 2012, **(c)** from 27 to 28 July 2012, **(d)** from 30 April to 4 May 2013, **(e)** 28 July 2013 and **(f)** 4 to 6 August 2013.

ACPD
15, 9507–9540, 2015

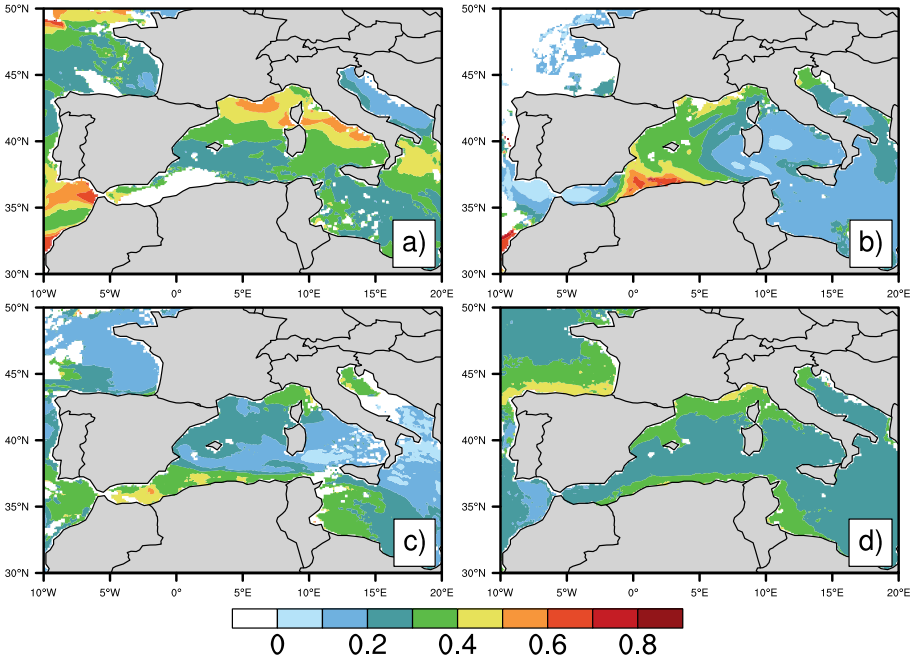

Figure 8. Mean daily SEVIRI AOD at 550 nm corresponding to identified pollution episodes at Cap Corse **(a)** for 26 March 2012, **(b)** 23 August 2012, **(c)** 6 September 2012, **(d)** from 13 to 20 July 2013.

ACPD
15, 9507–9540, 2015

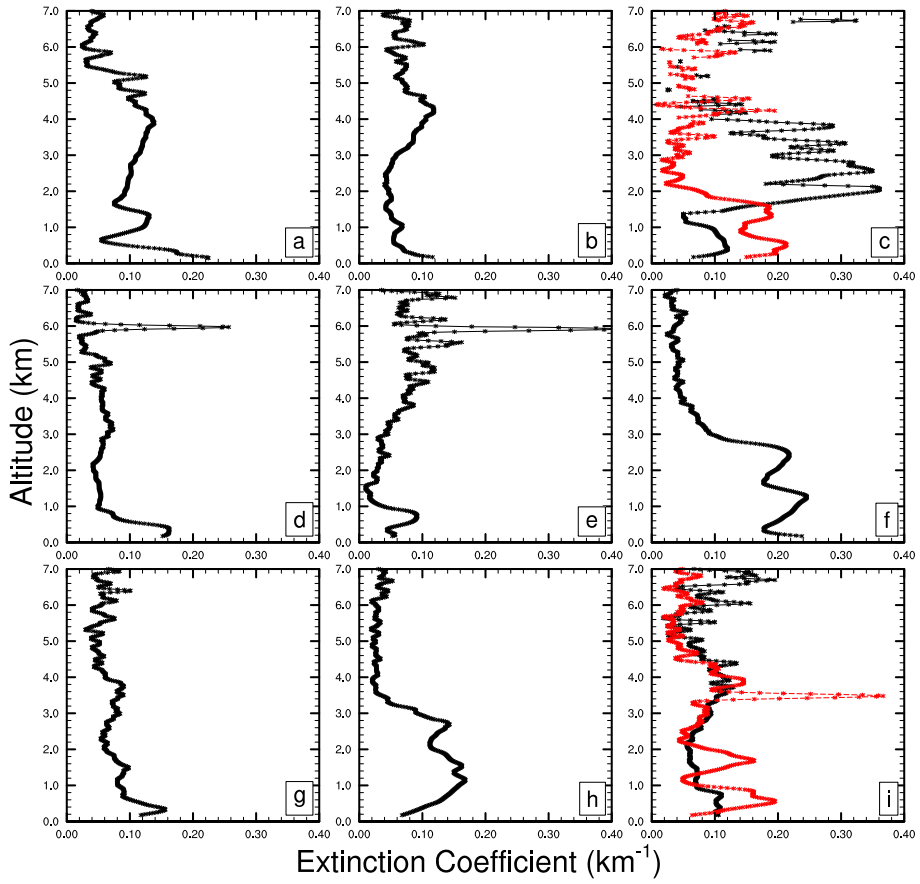

Figure 9. Vertical profiles of the aerosol extinction coefficient at 355 nm for selected events: **(a)** 29 June to 1 July 2012, **(b)** 27–28 July 2012, **(c)** 30 April (black solid line) and 2 May 2013 (red solid line), **(d)** 28 July 2013, **(e)** 4 August 2013, **(f)** 26 March 2012, **(g)** 23 August 2012, **(h)** 6 September 2012, and **(i)** 15 (black solid line) and 19 (red solid line) July 2013.

ACPD
15, 9507–9540, 2015

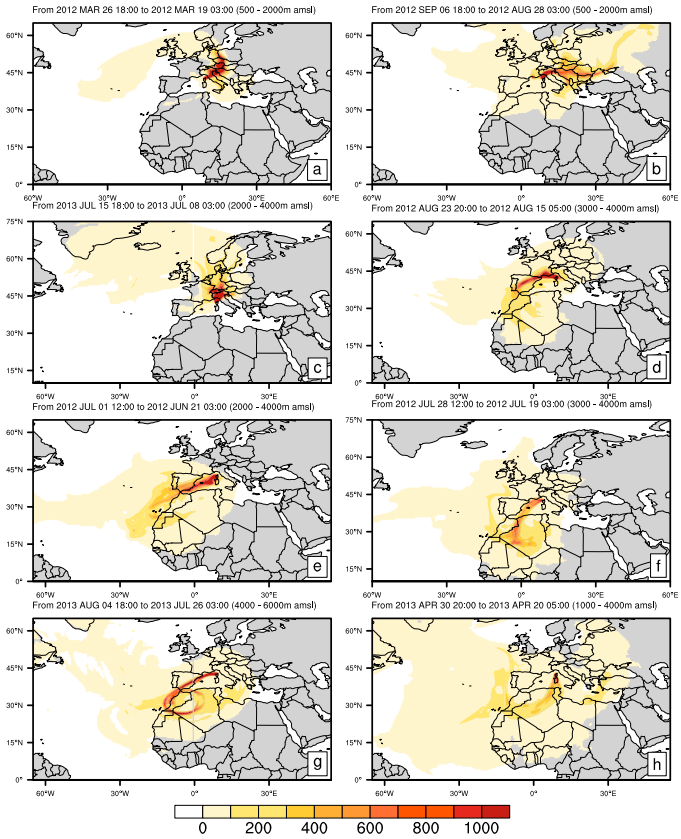

Figure 10. Backward simulations of the residence time for air masses (in seconds) arriving at Cap Corse using the Lagrangien particle dispersion model FLEXPART. The range of altitude for each release and the time period of the simulation are given at the top of each subplot labeled from **(a)** to **(h)**.

ACPD
15, 9507–9540, 2015